

Modelling droplet breakage in continuous emulsification using static mixers in the framework of entire spectrum of turbulent energy

Noureddine Lebaz¹, Fouad Azizi², Nida Sheibat-Othman^{1,*}

¹ University of Lyon, Université Claude Bernard Lyon 1, CNRS, LAGEPP UMR 5007, F-69100, Villeurbanne, France

² B.&W. Bassatne Department of Chemical Engineering and Advanced Energy, American University of Beirut, PO Box 11-0236, Riyad El-Solh, Beirut, Lebanon

Abstract

Droplets breakage during continuous emulsification in static mixers is investigated in this work. It is clearly shown that for viscous continuous phases, droplet breakage occurs mostly in the dissipation range of isotropic turbulence. To consider this, a modified breakage kernel of Coulaloglou and Tavlarides based on the full turbulence spectrum of Pope is employed within a population balance model to describe the time evolution of the droplet size distribution during the emulsification process. This full-spectrum-based model is tested against a wide range of experimental data and showed to be predictive and accurate. The full-spectrum-based model requires the knowledge of the mean turbulent kinetic energy and the mean energy dissipation rate that are obtained from computational fluid dynamic simulations (CFD). To allow a rapid implementation of the model without time-consuming CFD simulations, a model reduction is proposed based on mean energy dissipation rate estimation through pressure drop measurements only. The new model gives comparable predictive capabilities as that based on CFD simulations with improved computational efficiency.

* Corresponding author. Address: LAGEPP, Université Claude Bernard Lyon 1, bât 308G ESCPE-Lyon, 43 bd du 11 Novembre 1918, Villeurbanne 69622 France. Tel.: +33 04 72 43 18 50; Fax: +33 04 72 43 16 99
Email address: nida.othman@univ-lyon1.fr (Nida Sheibat-Othman)

1. Introduction

Emulsification processes allow dispersing one fluid into another immiscible fluid in the form of fine droplets. The breakage process is driven by energy dissipation, and stabilizing agents are frequently used to enhance the breakage by reducing the surface tension, and to avoid droplets recoalescence. The properties of the final liquid-liquid dispersion (e.g. mass transfer area, viscosity, or texture in food products) and its stability with time depend on the droplets size distribution (DSD). The production of these emulsions can be achieved in batch or in continuous modes, using stirred tank reactors, rotor-stators, high pressure homogenizers, membranes or static mixers. Static mixers are motionless in-line mixing elements that are usually inserted in a rigid pipe and they generate turbulence thanks to their specific geometrical structure, which disperses the fluid flow passing through the elements without any moving part. Emulsification through static mixers presents several advantages compared to the different processes introduced earlier. Indeed, in addition of operating in a continuous mode, static mixers offer an efficient homogenization of the fluids with low power requirements¹. This is not the case of stirred tanks, rotor-stators and high-pressure homogenizers which may lead to efficient but spatially heterogeneous breakage and with high energy consumption. Regarding continuous emulsification processes, such as membranes and hydrodynamic cavitation, they require relatively high pressure conditions ^{2,3}. This paper focuses on the use of SMX+ mixers in a continuous emulsification process.

When dealing with dispersed systems, the time evolution of the dispersed phase properties (e.g. size of the dispersed entities, chemical composition, temperature, etc.) can be represented by population balance models (PBMs) ⁴⁻⁶. This approach is preferred over mean property correlations because it gives access to the dynamic evolution of the entire distribution of the properties under investigation. PBMs were used to predict the DSD during

continuous emulsification by static mixers in different conditions. For instance, Azizi and Taweel (2011) modeled droplets breakage and coalescence of dilute oil-in-water emulsions in multi-stage screen-type static mixers ⁷. More recently, Lebaz and Sheibat-Othman (2019) investigated droplets breakage in SMX+ static mixers using a PBM and validated it against a wide range of experimental data ⁸, and compared the PBM prediction capability with a mean-size steady-state correlation ⁹. Since the energy dissipation rate inside the mixers plays a critical role during emulsification, computational fluid dynamics (CFD) is sometimes coupled with PBM in order to consider the local variation of the energy dissipation rate ¹⁰⁻¹³.

The population balance modelling of the droplets size in turbulent liquid-liquid systems relies on breakage and coalescence kernels, which describe the rate of these phenomena as a function of the physicochemical properties of the dispersed and continuous phases and the flow field properties. Most of the kernels available in literature employ the Kolmogorov turbulence energy spectrum model which is valid exclusively for the inertial subrange of isotropic turbulence, where the statistical properties of the turbulent flow are assumed to be only dependent on the local energy dissipation rate. Moreover, the Kolmogorov inertial range models are limited to fully developed turbulent flows in the infinite Reynolds number limit ¹⁴. Hence, the inertial subrange, where the Kolmogorov models are valid, becomes narrower for finite Reynolds number flows. This is the case when the continuous phase is highly viscous for instance. Moreover, as the size of droplets is distributed, part of the droplets may fall out of the limits of the inertial subrange. In such situations, one of the consequences of using classical kernels is the overestimation of the breakage and coalescence rates. Indeed, the energy of eddies is overestimated when the Kolmogorov model is extended over the energy-containing and the dissipation ranges ¹⁴.

For these reasons, recent studies focused on the extension of the kernels to the entire spectrum of isotropic turbulence. Solsvik and Jakobsen (2016) provided a literature survey on the modelling concepts of the turbulence energy spectrum and highlighted the limits of the Kolmogorov's model ¹⁵. Han et al. (2014) pointed out the necessity of considering the contribution of the full energy spectrum distribution in the breakage process ¹⁶. They compared the Kolmogorov model with the models based on the energy spectrum proposed by Pope (2001) ¹⁷ and Hinze (1975) ¹⁸ and found that the breakage frequency based on the entire energy spectrum of Pope agrees better with the experimental data of Andersson and Andersson (2006) ¹⁹ and Mass and Kraume (2012) ²⁰. Ghasempour et al. (2014) used the model of Pope to predict the number density of turbulent vortices in a turbulent pipe flow and validated it against a 3D vortex-tracking algorithm ²¹. Based on the model of Pope, Solsvik and Jakobsen (2016) proposed an approximate algebraic model to compute the second-order longitudinal structure function in order to reduce the computational cost for optimization and integral terms evaluation ¹⁴. So, they considered the integral scale Reynolds number dependency of the model parameters, unlike in Han et al. (2014) ¹⁶ and Ghasempour et al. (2014) ²¹ where constant parameters were employed. Later, Solsvik (2017) ²² proposed approximate explicit formulas that allow the calculation of the Pope's model parameters without the need for optimization. Niño et al. (2020) adopted a similar strategy to predict the bubble size distribution in an aerated tank, using a modified breakup and coalescence model that considers the entire cascade of turbulence ²³. They pointed out considerable improvements of bubble mean diameter predictions, which significantly influences mass transfer in the bioreactor. Karimi and Andersson (2018) ²⁴ selected well-known breakup kernels, initially derived for the inertial subrange of turbulence, in which they implemented the entire spectrum following the numerical approach proposed by Solsvik and Jakobsen

(2016)¹⁵. The predictions of the different breakage models were validated by two sets of experimental data reported in the literature^{19,25}. They concluded that including the entire spectrum of turbulent energy improves the predictive capability of the breakage kernels outside the inertial subrange. Later, Karimi and Andersson (2019)²⁶ considered all the disruptive (turbulent inertia and turbulent viscous shear) and cohesive (interfacial and internal viscous) stresses for the entire turbulent energy spectrum and their contributions to the breakage were evaluated. They showed that the breakage kernels of emulsions require the incorporation of all the stresses and the entire spectrum of turbulent energy, and ended up by establishing a regime map for different breakage mechanisms considering the length scales of vortices.

Castellano et al. (2019) proposed a model based on the second order structure function of Davidson (2015)²⁷ along with the Pope's energy spectrum to compute the breakage and coalescence rates, using the Coulaloglou and Tavlarides (1977)²⁸ framework²⁹. Besides, they implemented the volume-average kernels through the volumetric probability density function of the turbulent dissipation rate estimated by CFD simulations. They carried out experiments in a mechanically agitated liquid-liquid contactor at high continuous phase viscosity (up to 4.1 mPa.s) and found that the model was able to predict the experimental droplet Sauter mean diameter at different viscosities, turbulence conditions and dispersed phase volume fractions. The reliability of the above discussed extended models is tested against experimental data only in few cases. This is partly due to the novelty of this approach, but also because of its complexity. Indeed, this approach requires the knowledge of the turbulent kinetic energy and the energy dissipation rate that can be obtained from CFD simulations, while classical kernels only require the average energy dissipation rate that can be approximated by simple correlations. Another reason is due to the lack of valuable experimental data, especially in the

dissipative range. The contribution of this work is therefore two folds: The first objective is to validate the extended models over a wide range of experimental data, including experiments partly in the dissipative subrange of turbulence. Second, a simplified form of the full spectrum model is proposed to allow for its easier implementation without systematic heavy CFD simulations. The emulsification is achieved using SMX+ static mixers under diluted conditions to focus only on the breakage phenomenon. The breakage kernel of Coualoglou and Tavlarides (1977)²⁸ is employed in its modified form that accounts for the viscous forces in addition to the surface forces³⁰. This modified breakage kernel is extended to the entire energy spectrum using the model of Pope with the integral scale Reynolds number dependency of the model parameters and using the second order structure function of Davidson (2015) as suggested by Castellano et al. (2019)²⁹. In the second part, a simplified form of the model is proposed to enhance its implementation potential. To test the predictive capabilities of the breakage kernel proposed in this study, experiments are performed considering a wide range of energy dissipation and viscosities of the continuous and dispersed phases.

2. Theoretical aspects

2.1. Model description

The well-known Kolmogorov energy spectrum model is widely employed in the development of breakage kernels, and it assumes that breakage occurs exclusively in the inertial subrange of turbulence³¹. This model states that the turbulent energy is a monotonously decreasing function with the wavenumber κ of the eddies. In order to propose a model for the full turbulence spectrum, considering in addition of the inertial subrange the energy-containing and the dissipation ranges, Pope (2001) extended the Kolmogorov model by adding two

specified nondimensional functions (equations 1-3, Table 1): $f_L(\kappa L)$ which is related to the shape of the energy-containing range, and $f_\eta(\kappa\eta)$ relative to the dissipation range¹⁷. $f_L(\kappa L)$ and $f_\eta(\kappa\eta)$ tend to unity for large κL and small $\kappa\eta$ respectively, where L is the integral length scale of the largest eddies and η the Kolmogorov length scale, given by equations 4 and 5, respectively (Table 1). This ensures recovering the Kolmogorov model in the inertial subrange. The introduction of these two specific functions requires the determination of two adjustable parameters c_L and c_η from the two constraints on turbulent kinetic energy and its dissipation rate (equations 6 and 7, Table 1).

In isotropic turbulent flows, the breakage of fluid particles is related to the disruptive stresses of the continuous phase which need to be modelled. As discussed by Karimi and Andersson (2018), the second-order longitudinal structure function is generally used as an approximation of the mean fluctuating eddy velocity ($\bar{u}_\lambda^2 \approx \langle [\delta u]^2 \rangle(\lambda)$)²⁴. Based on the full turbulent energy spectrum of Pope, Davidson (2015) proposed a model of the second-order longitudinal structure function described in equation 8 (Table 1)²⁷. This model is adopted in this study.

Table 1: Summary of the energy spectrum model and population balance equations

Full turbulence spectrum of Pope ¹⁷	$E(\kappa) = C \varepsilon^{\frac{2}{3}} \kappa^{-\frac{5}{3}} f_L(\kappa L) f_\eta(\kappa \eta)$	(1)
Energy-containing range ¹⁷	$f_L(\kappa L) = \left\{ \frac{\kappa L}{[(\kappa L)^2 + c_L]^{1/2}} \right\}^{\frac{5}{3} + p_0}$	(2)
Dissipation range ¹⁷	$f_\eta(\kappa \eta) = \exp \left\{ -\beta \left([(\kappa \eta)^4 + c_\eta^4]^{1/4} - c_\eta \right) \right\}$	(3)
Integral length scale ¹⁷	$L = \frac{k^{3/2}}{\varepsilon}$	(4)
Kolmogorov length scale ³¹	$\eta = \left(\frac{u^3}{\varepsilon} \right)^{1/4}$	(5)
First constraint ¹⁷	$k = \int_0^\infty E(\kappa) d\kappa$	(6)

Second constraint ¹⁷	$\varepsilon = \int_0^\infty 2\nu\kappa^2 E(\kappa) d\kappa$	(7)
Second-order longitudinal structure function ²⁷	$\langle [\delta u]^2 \rangle(\lambda) = \frac{4}{3} \int_0^\infty E(\kappa) \left[1 + 3 \left\{ \frac{\cos(\kappa\lambda)}{(\kappa\lambda)^2} - \frac{\sin(\kappa\lambda)}{(\kappa\lambda)^3} \right\} \right] d\kappa$	(8)
Population balance equation ³²	$\frac{\partial n(v,t)}{\partial t} = \int_v^\infty b(v,v')g(v')n(v',t)dv' - g(v)n(v,t)$	(9)
Breakage kernel (full spectrum)	$g(d) = \frac{c_1 \sqrt{u^2(d)}}{d} \exp \left(-\frac{c_2 \sigma}{\rho_d d \sqrt{u^2(d)}} - \frac{c_3 \mu_d}{\rho_d^{3/2} \rho_c^{-1/2} d \sqrt{u^2(d)}} \right)$	(10)
Breakage kernel (inertial subrange) ²⁸	$g(d) = \frac{c_1 \varepsilon^{1/3}}{d^{2/3}} \exp \left(-\frac{c_2 \sigma}{\rho_d \varepsilon^{2/3} d^{5/3}} - \frac{c_3 \mu_d}{\rho_d^{3/2} \rho_c^{-1/2} \varepsilon^{1/3} d^{4/3}} \right)$	(11)
Breakage daughter size distribution ³³	$b(v,v') = \frac{60}{v'} \left(\frac{v}{v'} \right)^2 \left(1 - \frac{v}{v'} \right)^2$	(12)

For spatially homogeneous systems where the breakage phenomenon dominates, the time evolution of the DSD is given by the population balance equation 9 (Table 1). The first term on the right hand side of equation 9 accounts for the birth of droplets of volume v from bigger droplets of volume v' , and the second term is the death term describing the loss of droplets of volume v due to their breakage ³².

A continuous liquid-liquid emulsification process using static mixers is considered hereafter. Because of the low dispersed phase fraction and the use of a surfactant, droplets coalescence was found to be negligible ³⁴. Moreover, Ostwald ripening is not considered because of the negligible solubility of the employed oils in the aqueous phase. Hence, only droplets breakage occurs in the system. The breakage frequency (equation 11) is based on the Coualoglou and Tavlarides formalism with specific extensions in order to consider the contribution of the viscous forces to the cohesion of the droplets. This kernel is then adapted to handle the

occurrence of droplets disruption with respect to the entire energy spectrum of isotropic turbulence (equation 10, Table 1) (see Supporting Information for the developments). A beta daughter size distribution is considered (equation 12).

2.2. CFD simulations

Computational fluid dynamic (CFD) simulations of the process were achieved using the software ANSYS Fluent®. Single phase simulations were realized using the apparent viscosity of the emulsions, while varying the flow rate. A CAD drawing of a single SMX+ element of the correct dimensions was provided by Sulzer®. Simulations were done for 10 SMX+ elements as well as an upstream pipe section equivalent to 3 pipe diameters and a downstream pipe section equivalent to 10 pipe diameters. Mean mass and momentum conservation equations were solved for a steady state, incompressible and Newtonian fluid flow using a finite-volume solver (ANSYS Fluent®). A fully developed laminar velocity profile was imposed at the inlet of the pipe while the outlet was set to the outflow boundary condition. Regarding the solid walls of the mixers and the rigid pipe, a non-slip boundary condition was imposed. The SIMPLE (Semi-Implicit Method for Pressure Linked Equations) algorithm was used for pressure-velocity coupling and the QUICK (Quadratic Upstream Interpolation for Convective Kinematics) scheme was employed for spatial discretization. The convergence criteria were set to 10^{-6} .

To solve for the turbulent flow inside the mixers the realizable $k-\varepsilon$ model was employed because it is suitable to complex shear flows involving strong streamline curvature conditions. This required imposing a turbulence intensity and a length scale at the inlet. The former was fixed to a low turbulence intensity value of 1 % while the latter was set equal to the pipe diameter. A grid sensitivity analysis was performed using the Grid Convergence Index (GCI)

method³⁵ and it was found that approximately 5.4 million cells for each SMX+ element were required to reach a GCI < 2% for either the pressure drop or turbulent energy dissipation parameters.

From these simulations, it appeared that the volume-average energy dissipation in each mixer reaches hydrodynamic equilibrium in the second SMX+ element where its value becomes constant for all subsequent downstream elements. Therefore, volume-average values of energy dissipation were calculated for the first mixing element ($\bar{\varepsilon}_1$), second to tenth elements ($\bar{\varepsilon}_2$) and in the downstream section ($\bar{\varepsilon}_3$), which was defined as having a length equivalent to 2 pipe diameters downstream of the last mixer. These average values are shown in Table 2. With the different flow rates, the residence time varies between 0.025 to 0.4 s in the whole system (including the 10 mixing elements and the empty pipe sections).

2.3. Numerical details

For the determination of the two adjustable parameters c_L and c_η , the non-linear constraints (equations 6 and 7 in Table 1) are solved numerically using the Matlab® function *fsolve* with the function *integral* to compute the integral terms. The function *fsolve* is based on the Trust-Region Dogleg method while the function *integral* computes numerical integration using adaptive quadrature and default error tolerances. To compute the integral within the second-order longitudinal structure function (equation 8), the function *ode45* is employed for a better numerical stability, which is a non-stiff differential equations solver based on explicit Runge-Kutta (4,5) formula.

Regarding the PBM, the finite volume method of Kumar et al. (2009) is adopted to solve the partial differential equation³⁶. Technical details on this solution method may be found in their original article.

3. Materials and experimental methods

3.1. Emulsion ingredients

Ultrapure water obtained using a Synergy unit system (Millipore, France) is mixed with different proportions of Glycerol (VWR Chemicals, France) to get a continuous phase with different viscosities (Table 2). Polysorbate 20 (Tween20®, supplied by Sigma-Aldrich, Germany) is used as surfactant and is dissolved in the continuous phase (about 5 g/L). Silicon oils (Bluestar Silicone, France) of different viscosities are dispersed in the glycerol-water mixture to form the oil-in-water pre-emulsions.

3.2. Experimental setup and emulsification procedure

The experimental set-up used in this study is similar to that described in Lebaz and Sheibat-Othman (2019)⁹ (Figure 1). First, pre-emulsions are prepared in a stirred tank by mixing silicon oil with water/glycerol blends during 2 hours at 500 rpm, using a Rushton turbine. The pre-emulsions are then pumped through the static mixers using an MCP-Z Ismatec® gear pump. The pressure drop induced mainly by the presence of the static mixers is measured using a pressure gauge (Keller LEO1: 0-3 bar, ±3 mbar, Germany). At the inlet and the outlet of the mixers, samples are taken and the DSD is measured off-line by a laser diffraction particle size analyzer (Mastersizer 3000, Malvern Instruments, France) after dilution of the emulsions in pure water. Each measurement is repeated three times and the average DSDs are shown the results section.

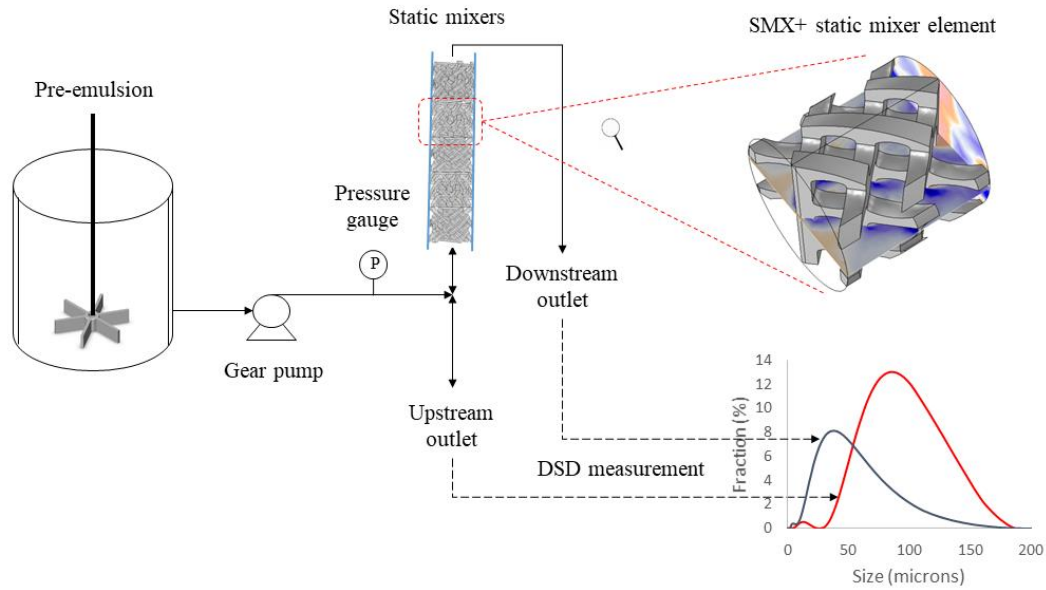


Figure 1: Schematic representation of the experimental setup employed for the preparation of emulsions using SMX+ static mixers

Table 2 gives the list of experiments carried out and their specifications. The hydraulic Reynolds number is given by $Re_h = \rho u_s D_h / (\varphi \mu)$, with u_s the superficial velocity, φ the porosity of the mixers, D_h the mixer hydraulic diameter and ρ and μ the apparent density and viscosity of the continuous phase³⁷. For turbulent emulsification, Re_h should be higher than 260³⁸. The experiments with $\mu_c > 1$ mPa.s are all performed at the same hydraulic Reynolds number, whereas those at $\mu_c = 1$ mPa.s are realized at higher Re_h to ensure relatively significant droplet breakage in the mixers.

Table 2 : List of experiments carried out by varying the viscosity of the continuous/dispersed phases and the Reynolds number. In all the experiments, 10 SMX+ elements were used with pre-emulsions prepared in the same conditions (mixing for 2 hours at 500 rpm).

Exp. n°	Water (wt%)	Glycerol (wt%)	μ_c [mPa.s]	μ_d [mPa.s]	Re_h	$\bar{\epsilon}$ [m ² s ⁻³] (from CFD)			$\bar{\epsilon}$ [m ² s ⁻³] (from ΔP)
						$\bar{\epsilon}_1$	$\bar{\epsilon}_2$	$\bar{\epsilon}_3$	
1	100	0	1	20	1092	164	248	32	264
2	100	0	1	100	1092	164	248	32	296
3	100	0	1	200	1093	164	248	32	264
4	100	0	1	50	1239	250	407	53	407
5	100	0	1	50	1387	296	483	64	595
6	100	0	1	50	1680	561	922	124	1013
7	54.3	45.7	5	5	272	331	413	45	651
8	54.3	45.7	5	10	272	331	413	45	700
9	54.3	45.7	5	50	271	331	413	45	656
10	54.3	45.7	5	100	271	331	413	45	633
11	46.7	53.3	7.5	5	282	1167	1463	162	2258
12	46.7	53.3	7.5	10	282	1167	1463	162	2074
13	46.7	53.3	7.5	50	281	1167	1463	162	2054
14	46.7	53.3	7.5	100	280	1167	1463	162	2004
15	42.2	57.8	10	5	282	2659	3332	370	3979
16	42.2	57.8	10	10	281	2659	3332	370	4107
17	42.2	57.8	10	50	280	2659	3332	370	3994

18	42.2	57.8	10	100	280	2659	3332	370	4066
----	------	------	----	-----	-----	------	------	-----	------

4. Results and discussion

4.1. Necessity of extended breakage kernels

To point out the necessity of extending the classical breakage kernels over the entire energy spectrum of isotropic turbulence in the case of emulsification using static mixers, the computed energy spectrum is plotted against the wavenumber κ for different experiments with a superposition of the particle volume-based mean size D_{43} and the DSD percentiles D_{10} and D_{90} at the inlet of the mixers. Figure 2 represents a comparison between two experiments carried out at different viscosities of the continuous phase (left: Experiment n° 2 at $\mu_c = 1$ mPa.s, right: Experiment n° 17 at $\mu_c = 10$ mPa.s). The inertial subrange is delimited by the integral length scale of the largest eddies with a factor 0.5 on one side, and by the Kolmogorov length scale with a factor 15 on the other side ²⁴.

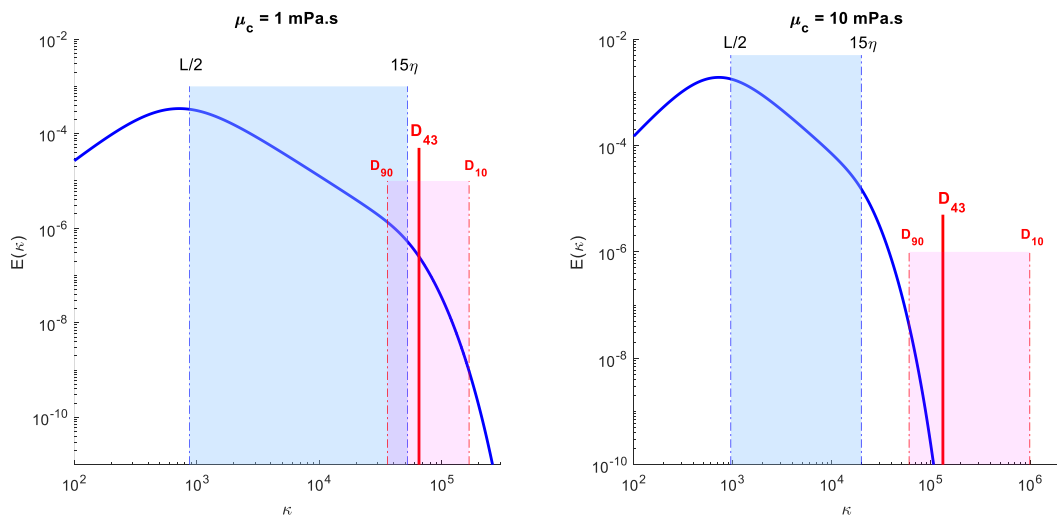


Figure 2: Energy spectrum with inertial subrange limits ($0.5 L - 15 \eta$) and the location of the droplet size distribution for different continuous phase dynamic viscosities μ_c . Left: Continuous phase with a low viscosity (experiment 2). Right: Continuous phase with a high viscosity (experiment 17).

First, it can be seen that the increase of the continuous phase viscosity reduces the interval of validity of the inertial subrange. Second, smaller droplets are produced when using a higher continuous phase viscosity, under the considered operating conditions. The location of the DSD at the inlet of the static mixers is reported in the two cases by the means of the volumetric mean diameter and the two percentiles D_{10} and D_{90} . In the first case (left), where the continuous phase viscosity is low, the mean diameter of the DSD (D_{43}) is close to the lower limit of the inertial subrange of isotropic turbulence, so part of the droplets falls in this subrange of eddies, while the other part is within the dissipation range. In the second case (right), where the continuous phase viscosity is higher, the mean diameter of the DSD is far from the inertial subrange, and the entire DSD falls within the dissipation range. This short analysis demonstrates the necessity of extending the breakage kernels to the entire spectrum of isotropic turbulence instead of using the classical formulations which assume droplet breakage occurring exclusively within the inertial subrange of turbulence.

4.2. Energy spectrum model simplification

As shown in Figure 2, in the case of emulsification process in SMX+ static mixers, the DSD is mostly in the dissipation range whatever the continuous phase viscosity, with the operating conditions considered in this work. As explained earlier, the Pope's model of turbulent energy spectrum is based on the modification of the turbulent energy model of Kolmogorov by adding two specific nondimensional functions $f_L(\kappa L)$ and $f_\eta(\kappa\eta)$, related to energy-containing and dissipation ranges respectively. The behavior of these two functions is shown in Figure 3.

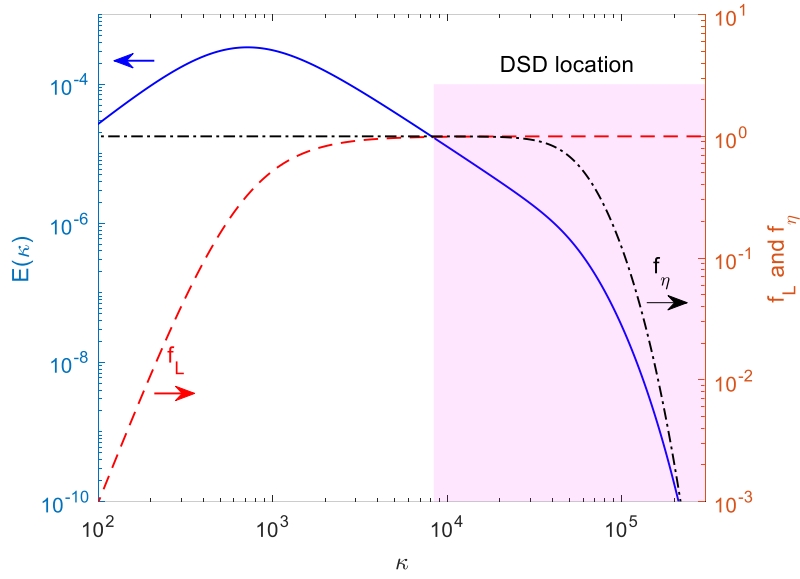


Figure 3 : Energy spectrum of Pope with the two nondimensional functions f_L and f_η shown for the experiment 2.

As expected, the function $f_L(\kappa L)$ tends towards unity in the region of the spectrum where the DSD is located. Hence, the Pope's model in the case of emulsification in SMX+ mixers may be simplified as follows:

$$E(\kappa) = C \varepsilon^{\frac{2}{3}} \kappa^{-\frac{5}{3}} f_\eta(\kappa \eta) \quad (13)$$

This simplification reduces the computational cost since only one adjustable parameter c_η should be determined using the non-linear constraint given by equation (7). More interestingly, only the mean energy dissipation rate $\bar{\varepsilon}$ is needed in this case, and it is no more required to compute the mean turbulent kinetic energy, k . This means that the model may be implemented without CFD simulations of the system. Indeed, in many systems, there are some correlations allowing to approximate reasonably the mean energy dissipation rate that can be used in the kernel. This is not the case when considering the entire model since it is based on both the turbulent kinetic energy and its dissipation rate.

4.3. Parameter identification strategies

The identification of the breakage kernel parameters was achieved using the following criterion:

$$\min_{C_1, C_2, C_3} J = \sum_{k=1}^M |q_e(v, k) - q_m(v, k)| \quad (14)$$

Where $q = v n \Delta v$ is the volume fraction distribution of droplets at the outlet of the mixers and M the number of experiments used for identification. The index 'e' refers to the experimental measurements while the index 'm' refers to the model predictions. The *Multistart* and *lsqnonlin* Matlab® functions (Optimization Toolbox) were employed. The *Multistart* function is preferred to avoid convergence towards a local minimum. The function *lsqnonlin* is a nonlinear least-square solver based on the trust-region-reflective algorithm.

In order to ensure global parameter estimation, two identification strategies were compared. In the first strategy, all available experiments were used for parameter identification (i.e. $M = 18$). So, the criterion to be minimized includes the differences between the outlet measured DSD in volume and the model predictions for all experiments. The advantage of this strategy is that it allows to have the best compromise of parameters that fit best all the experiments. The disadvantage is that experiments with errors may impact the identification equally as truthful experiments. By this strategy, it quickly appeared that $C_3=0$, which is coherent with previous results of emulsification in static mixers⁹. This can be explained by the fact that at high and relatively uniform energy dissipation rate observed in the mixers, the disruptive turbulent energy needs to overcome the interfacial energy, while the viscous forces of the droplet become negligible. Therefore, the procedure was repeated by eliminating C_3 from the model. The identified parameters by this strategy are shown in Table 3 for the full spectrum and the inertial-based models.

The second strategy consists of iteratively selecting three experiments for parameters identification until covering all the possible combinations among the available experiments and then examining the histogram of the identified parameters. The advantage of this strategy is that it allows eliminating experimental errors (e.g. measurement error of the DSD) as their occurrence is not regular, and one may easily detect them and analyze their coherence. By this strategy, it appeared that one should be careful about the choice of the experiments used for identification as a wide range of parameter values could be obtained. However, most triads of trustful experiments converged to parameters close to those found in the first strategy. Hence, the parameters resulting from the first strategy will be used for model validation and comparison between the full spectrum and the inertial subrange-based models in the following sections.

Table 3: Identified breakup kernel parameters for both models using all available experiments (and $\bar{\epsilon}$ evaluated by CFD).

	C₁	C₂
Inertial subrange-based model	1.37×10^{-3}	3.19×10^{-2}
Full spectrum-based model	5.12×10^{-4}	4.56

4.4. Predictive capabilities of the two models

The predictions of the inertial subrange-based model (equation 11) and the full spectrum-based-model (equation 13) for the different experiments are detailed in this section, under different operating conditions. The figures are assembled regarding the viscosity of the continuous phase.

Let us first have a look on the mechanism of droplet breakage in the mixed vessel during the pre-emulsion preparation step, which appears on the inlet DSDs. Two mechanisms can be

distinguished and seem to occur depending on the ratio μ_d/μ_c : When $\mu_d/\mu_c > 1$, the pre-emulsions show a monomodal DSD with an increasing mean droplet size for higher μ_d . As the ratio μ_d/μ_c decreases, a transition from a monomodal to a bimodal distribution is observed (see Figures 4, 5 and 6). A similar observation was reported by Carrillo de Hert and Rodgers^{39,40}, but for emulsification using highly viscous oils. This seems to be mainly due to the non-uniformity of energy dissipation in the stirred vessel, with a high local shear near the impeller and a much lower energy dissipation in the rest of the vessel, thus leading to two populations of different sizes. A second reason could be due to the daughter size distribution that changes with the ratio μ_d/μ_c from normal or bell-shape to U-shape, where small droplets are formed following an erosion-like mechanism. This however seems to represent a minor effect as it can hardly justify the big difference in size between the two populations. Note that in the static mixers, the energy dissipation rate is more uniform thanks to the regular flux crisscrossing within the reduced free volume of the mixers. Therefore, whatever the inlet DSD form (monomodal or bimodal), the same outlet form is obtained, but with smaller droplets.

Figures 4-7 also allow to compare the predictions by the two breakage models (inertial subrange and full spectrum), using the parameters identified in Table 3. As a general remark, the two models are capable of predicting the outlet DSD with a very good accuracy for the different explored conditions: Changes of the inlet DSD, viscosities of the dispersed/continuous phases and mean energy dissipation rate. The predictions accuracy is similar for both models except for the highest viscosity of the continuous phase (Figure 7) where the full spectrum-based model is slightly more accurate. Indeed, as explained in Figure 2, the importance of using the full spectrum model is increased when the DSD falls out of the inertial subrange, which is the case when droplets are much smaller or when increasing the viscosity of the continuous phase. To be fully within the inertial subrange, the energy

dissipation rate should be lower which may be achieved by reducing the flow rate through the mixers. However, for the experiments done at $\mu_c = 1$ mPa.s for instance (Figure 4), when the hydraulic Reynolds number (Re_h) was set equal to that of experiments at higher viscosity (Table 2), no droplet breakage occurred and the DSD at the outlet of the mixers was the same as at the inlet (results not shown). Therefore, Re_h was set at least five times higher for these experiments, compared to the experiments at $\mu_c > 1$ mPa.s. Even at such high Re_h , droplets breakage is low as shown in Figure 4 (especially in the subfigures at the minimal $\bar{\epsilon}$).

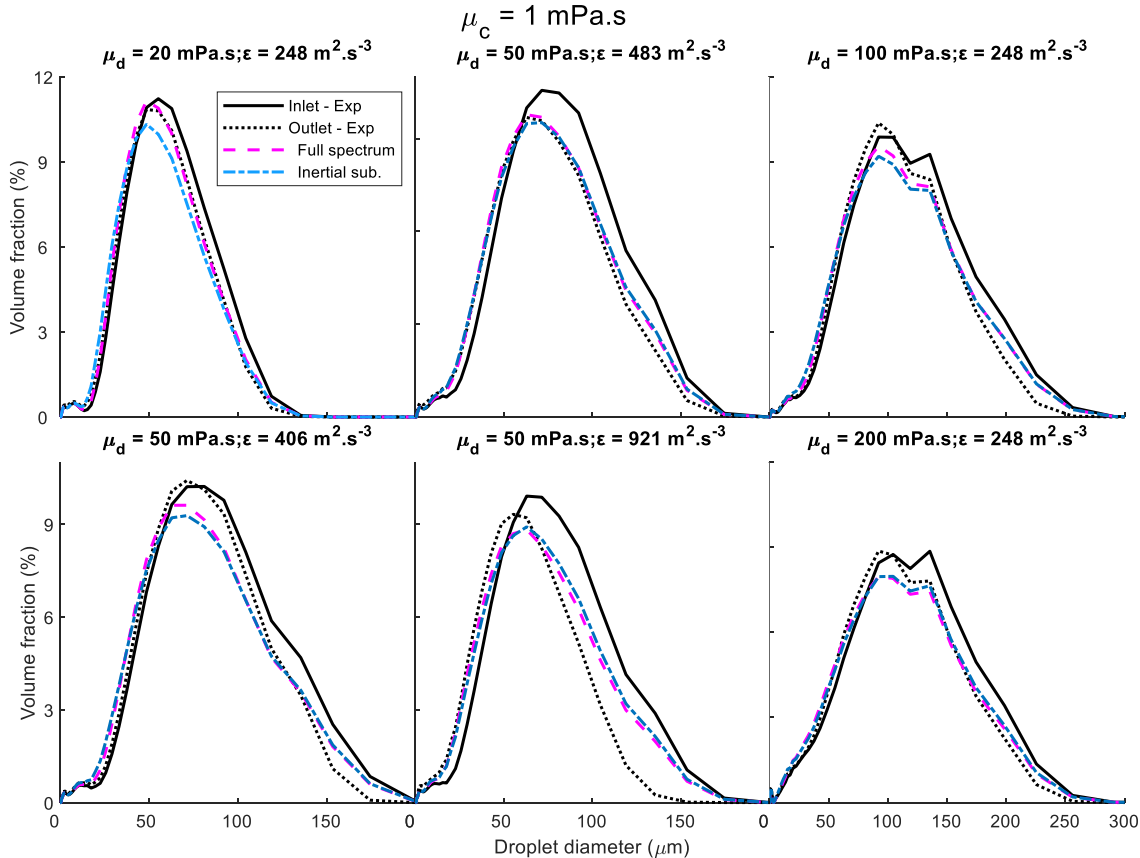


Figure 4: DSD predictions at the outlet of the mixers for the inertial subrange-based model (dotted blue lines) and the full spectrum-based model (dashed magenta lines) at $\mu_c = 1$ mPa.s and different viscosities of the dispersed phase and mean energy dissipation rate ($\bar{\epsilon}_2$). Comparison with experimental data (inlet: black line; outlet: dashed black line)

The similar predictive capability of the two models is mainly explained by the fact that both models were identified for all the experiments. However, in view of the indication that the DSD location at the inlet of the mixers is in big part within the dissipative range of turbulence for all the cases (as schematically explained in Figure 2), the full spectrum model is more appropriate to use. The lack in correct physics of the inertial subrange-based model seems therefore to be compensated by the numerical identification over the set of experiments. But, the full spectrum-based model and its parameters can be believed to be fundamentally more coherent. This situation also explains why over the last decades, PBM developments were focused on the interaction mechanisms instead of questioning the validity of the energy spectrum model assumption.

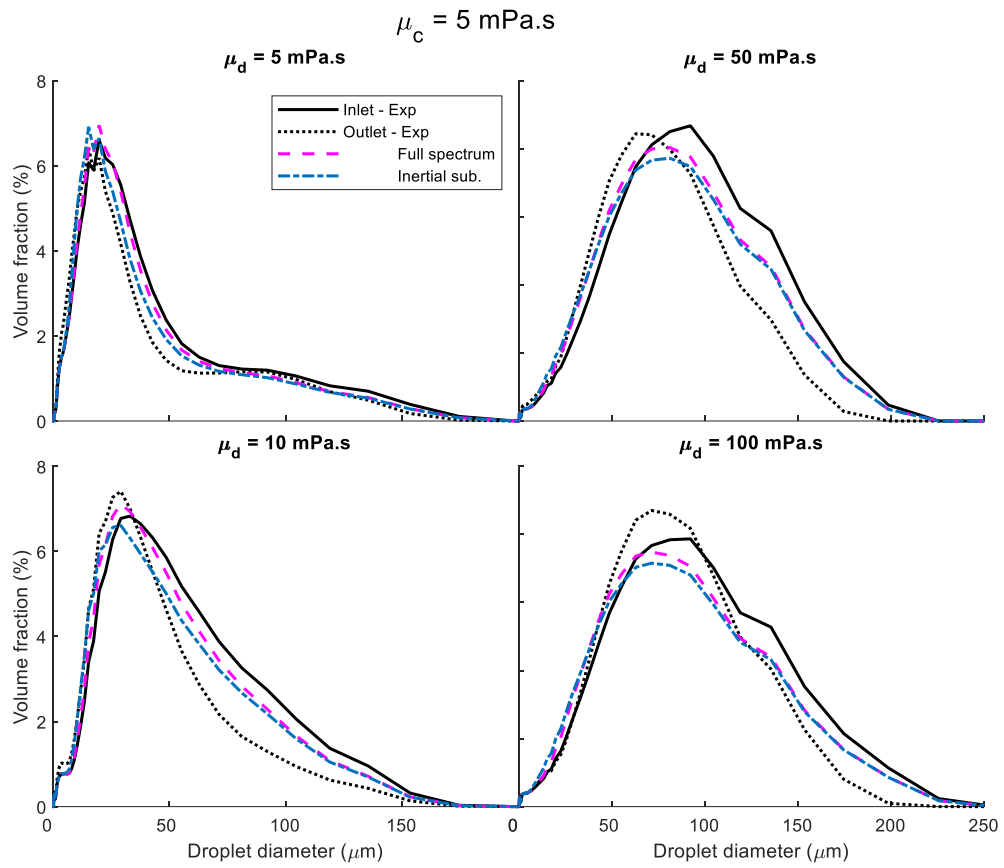


Figure 5: DSD predictions at the outlet of the mixers for the inertial subrange-based model (dotted blue lines) and the full spectrum-based model (dashed magenta lines) at $\mu_c = 5 \text{ mPa.s}$ and different viscosities of the dispersed phase.

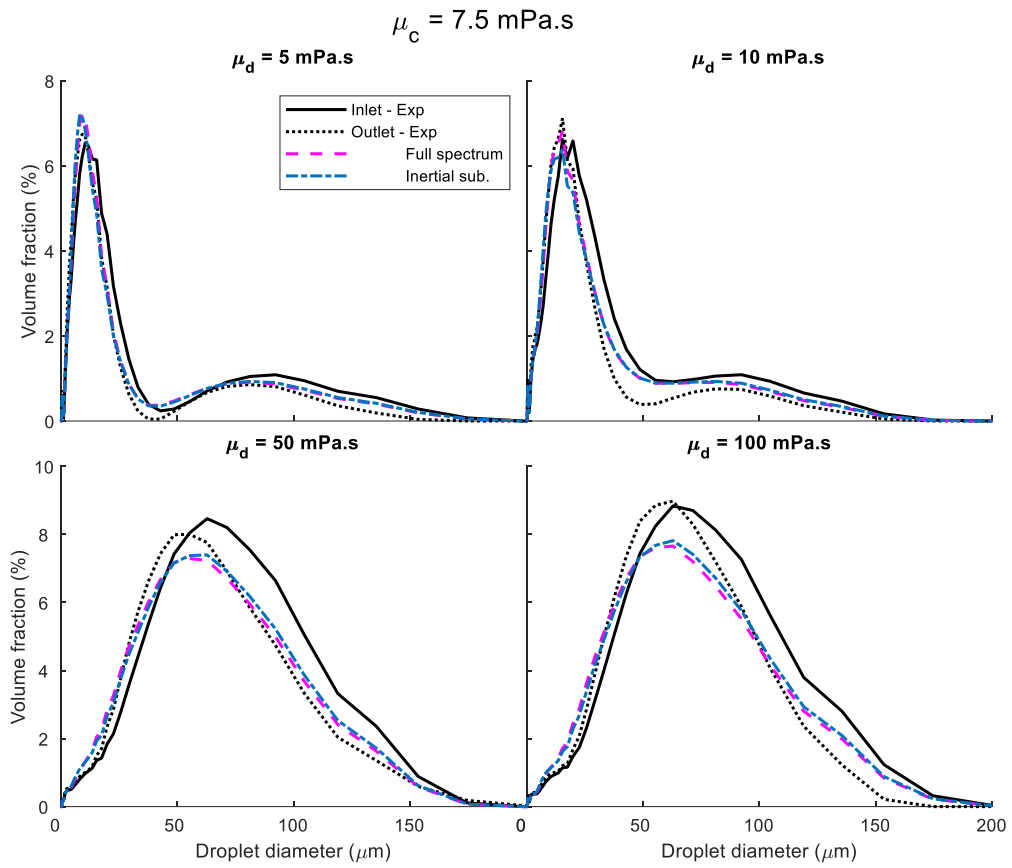


Figure 6: DSD predictions at the outlet of the mixers for the inertial subrange-based model (dotted blue lines) and the full spectrum-based model (dashed magenta lines) at $\mu_c = 7.5 \text{ mPa.s}$ and different viscosities of the dispersed phase.

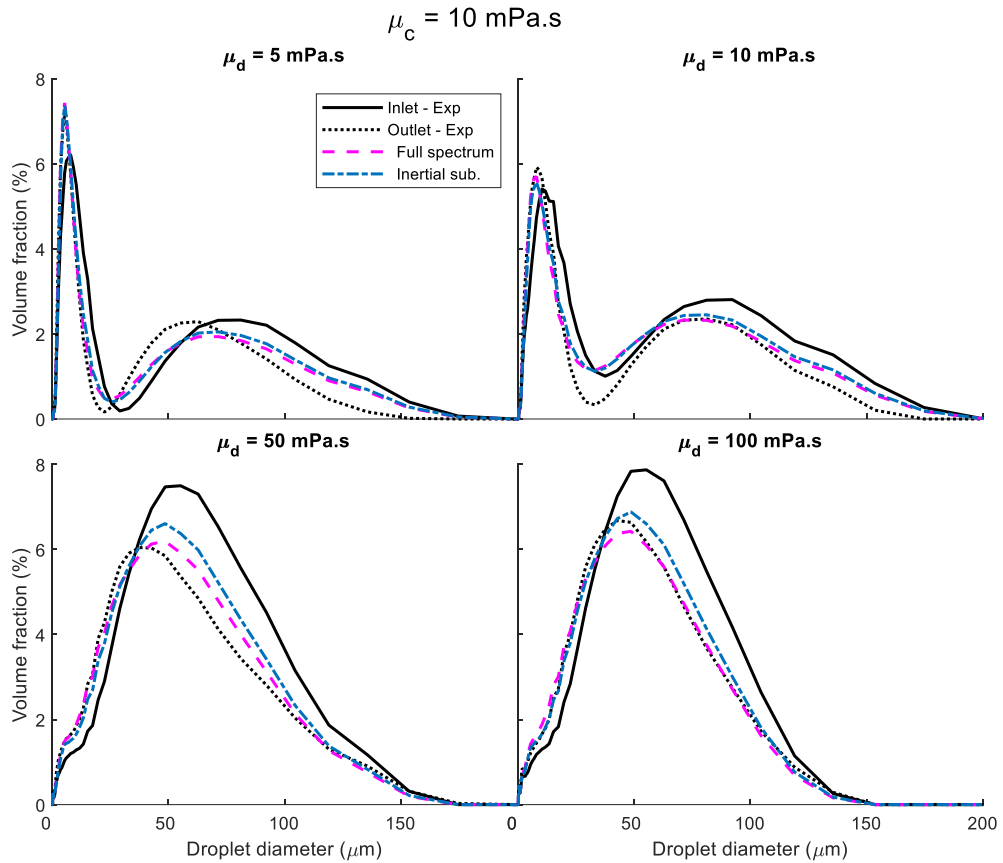


Figure 7: DSD predictions at the outlet of the mixers for the inertial subrange-based model (dotted blue lines) and the full spectrum-based model (dashed magenta lines) at $\mu_c = 10$ mPa.s and different viscosities of the dispersed phase.

In order to demonstrate the need of the full spectrum model and its better capability to predict data out of the identification set, another identification strategy was followed: The two models were identified only using experiments done at $\mu_c = 1$ mPa.s, then used to predict the evolution at higher μ_c . Therefore, the six first experiments in Table 2 were used to identify the full spectrum model. For the inertial subrange-based model, besides these 6 experiments, other experiments reported in our previous work⁹ were employed (a total of 15 experiments). Then, the two models, with their identified parameters (C_1 and C_2), were used to predict the evolution of the outlet DSD in the case of higher μ_c ($\mu_c = 10$ mPa.s).

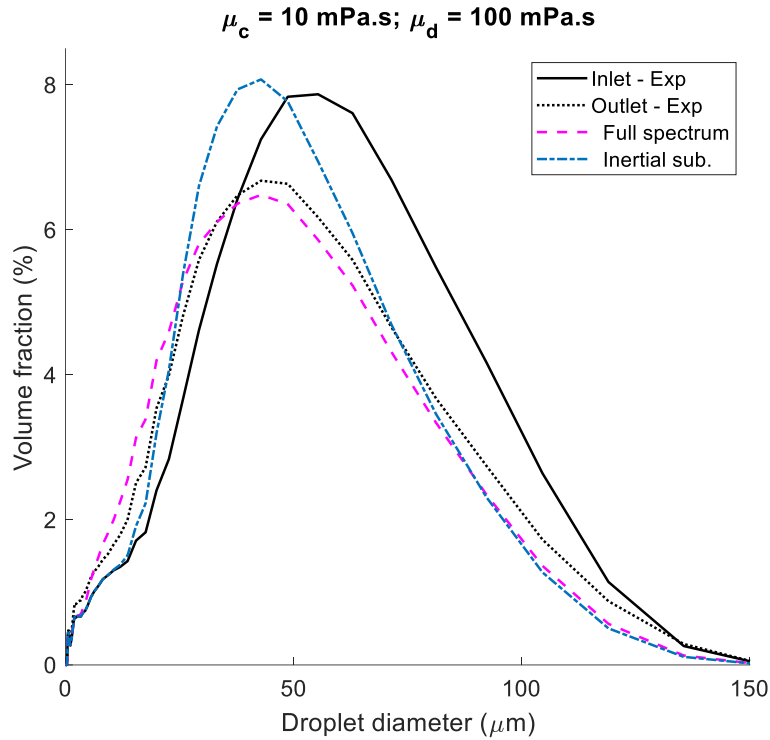


Figure 8: DSD predictions at the outlet of the mixers for the inertial subrange-based model (dotted blue lines, $C_1=3.51 \times 10^{-3}$ and $C_2=5.76 \times 10^{-1}$) and full spectrum-based model (dashed magenta lines, $C_1=7.81 \times 10^{-4}$ and $C_2=8.07$) at $\mu_c = 10 \text{ mPa.s}$ at $\mu_d = 100 \text{ mPa.s}$. Here, for both models, parameter identification is only based on experiments with $\mu_c = 1 \text{ mPa.s}$.

As shown in Figure 8, the predictions of the full spectrum-based model are more accurate than the inertial subrange-based model. Both models slightly overestimate the breakage of large droplets, but the inertial subrange-based model also underestimated the breakage of small droplets. The predictive capability of the full spectrum model is therefore higher than the inertial subrange-based model. This example illustrates the issues facing the classical breakage kernels when their domain of validity is not respected, and the importance of the set of experiments used for parameter identification.

4.5. Predictions by the simplified model

In the previous sections, the full spectrum model (equation 1) was evaluated and was compared to the inertial subrange-based model. In both models, the energy dissipation rate

was estimated through CFD simulations. In this section, the simplified model (equation 13) is investigated. One of the main advantages of this model is that it does not necessitate CFD simulations, as it only requires the mean energy dissipation rate which can be obtained easily in different devices using simple correlations. In the case of emulsification using static mixers for instance, the mean energy dissipation rate may be estimated experimentally from pressure drop measurements (ΔP) as follows ⁴¹:

$$\bar{\varepsilon} = \frac{\Delta P u_i}{\rho L_s} \quad (15)$$

The interstitial velocity, u_i , can be calculated from the superficial velocity, u_s , and porosity of the mixers, φ , as follows:

$$u_i = \frac{u_s}{\varphi} = \frac{4 Q}{\pi D_s^2} \frac{1}{\varphi} \quad (16)$$

The calculation of $\bar{\varepsilon}$ through the measurement of pressure drop makes the modelling approach accessible compared to the full spectrum models proposed in literature where CFD simulations are mandatory to get access to the turbulent kinetic energy and its dissipation rate. This experimental value of $\bar{\varepsilon}$ is then implemented in both models (the simplified full spectrum model and the inertial subrange-based model), and their predictions are investigated. The same global parameter identification procedure is employed as previously discussed and the identified parameters are given in Table 4. The slight difference between the parameters identified in this table compared to Table 3 are due to differences in the evaluation of $\bar{\varepsilon}$ (by CFD or experimentally). For instance, when employing the CFD, slightly different values of $\bar{\varepsilon}$ were obtained in the first mixer compared to the 9 following ones, while in the pressure drop method we only get one mean value of $\bar{\varepsilon}$. However, it can be seen that the parameters remain comparable. Only the value of C_1 of the full spectrum-based model

changed noticeably, from 5.12×10^{-4} to 1.09×10^{-3} . The prediction capability of the two models is illustrated in Figure 9 for different μ_c .

Table 4: Identified breakup kernel parameters for both models using all experiments based on the mean energy dissipation rate estimated through pressure drop.

	C₁	C₂
Inertial subrange-based model	1.33×10^{-3}	4.20×10^{-2}
Simplified full spectrum-based model	1.09×10^{-3}	4.69

It can be seen that the predictions of the two models are similar and in good agreement with the experimental DSDs in the different experiments. They are comparable to the predictions obtained using both models (full spectrum or inertial subrange) based on CFD simulations to estimate $\bar{\varepsilon}$. This demonstrates that when an estimation of the mean turbulent dissipation rate through experimental measurements is possible, the full spectrum-based model may be implemented easily without realizing time-consuming CFD simulations. Note that this is coherent in systems showing mostly uniform energy dissipation rate within the entire volume of the process, which is rather valid in static mixers. A criterion can be defined to determine when the simplified model is applicable, based on the energy dissipation and the droplet size. From Figure 2, if $\kappa > \frac{L}{2}$, then the size of droplets falls within the inertial and/or dissipation subranges of turbulence. Based on the definitions, $L = k^{3/2}/\varepsilon$ and $\kappa = 2\pi/D$, the following criterion is required to ensure the validity of the simplified model:

$$D < \frac{4\pi\varepsilon}{k^{3/2}} \quad (17)$$

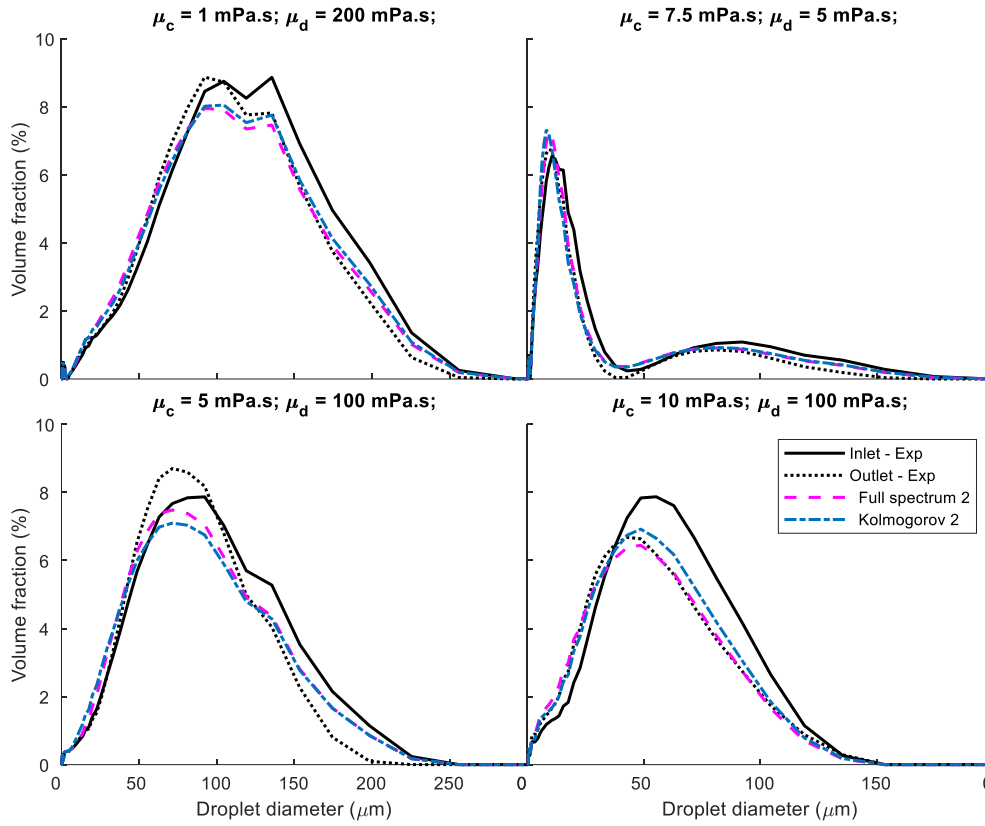


Figure 9: DSD predictions by the inertial subrange-based model (dotted blue lines) and the simplified full spectrum-based model (equation 13) (dashed magenta lines) at different dispersed/continuous viscosities using the energy dissipation rate evaluated through pressure drop measurements.

5. Conclusion

Modelling of the continuous emulsification process in static mixers is investigated in this work in the case of viscous continuous phase fluids. A population balance model accounting for droplets breakage mechanism that covers both the inertial and the dissipation subranges of turbulence is derived. Two forms of this model were proposed: its complete form and a simplified form. This model was also compared to a classical model which assumes that breakage occurs exclusively within the inertial subrange of turbulence.

First of all, the model of Pope is employed as a basic framework for the modelling of the full energy spectrum of isotropic turbulence. Indeed, based on experimental results, it is shown

that in the case of emulsification using SMX+ static mixers, droplet breakage occurs in the dissipation and inertial subranges of turbulence, which necessitates the use of a full spectrum model. The first full spectrum form of the model relies on two parameters that need to be estimated, which require the mean energy dissipation rate and the kinetic turbulent energy, obtained by CFD simulation. The simplified form of the full spectrum model relies only on one parameter. Indeed, a careful analysis of the parameters of the energy model shows that the function $f_L(\kappa L)$ tends towards unity in the region of the spectrum where the DSD is located. Hence, the model of Pope is simplified to consider only the inertial and dissipation subranges (and not the energy containing subrange) which requires the determination of only one model parameter through the knowledge of the mean energy dissipation rate. For this, an experimental evaluation of the energy could be done based on the pressure drop measurement, without using CFD simulations, which represents a valuable advantage of the proposed model.

First, the prediction capability of the full spectrum model is compared to that of a classical model. The parameters of both models were identified identically. The two models give very good predictions for the different explored conditions with comparable accuracy. However, the full spectrum model is shown to be more robust for the prediction of the DSD out of the optimization domain.

Second, the simplified full spectrum model was investigated. To avoid the use of complex and time consuming CFD simulations to estimate the mean energy dissipation rate, an alternative is proposed through its experimental estimation based on pressure drop measurement. It is demonstrated that using this procedure does not alter the predictive capabilities of the developed model. The applicability of the simplified full spectrum model is therefore as straightforward as classical kernels.

Nomenclature

$b(v, v')$	Breakage daughter size distribution	m^{-3}
C	Kolmogorov constant (equation 1, $C = 1.5$)	-
c_i, C_i	Constants	-
c_L	Large-scale constant of the Pope's model	-
c_η	Dissipative-scale constant of the Pope's model	-
d	Droplet diameter	m
D_h	Hydraulic diameter of the mixer	m
D_s	Diameter of the pipe	m
D_{43}	Volume-based mean droplet size	m
E_{crit}	Critical energy	$\text{kg m}^2 \text{s}^{-2}$
$E(\kappa)$	Energy spectrum	$\text{m}^3 \text{s}^{-2}$
E_s	Surface energy	$\text{kg m}^2 \text{s}^{-2}$
\bar{E}	Eddies turbulent energy	$\text{kg m}^2 \text{s}^{-2}$
E_v	Viscous energy	$\text{kg m}^2 \text{s}^{-2}$
f_L	Large-scale function of the Pope's model	-
f_η	Dissipative-scale function of the Pope's model	-
$g(v)$	Volume-based breakage frequency	s^{-1}
J	Objective function	-
k	Turbulent kinetic energy	$\text{m}^2 \text{s}^{-2}$
L	Integral length scale of the largest eddies	m
L_s	Length of the pipe	m
M	Number of experiments	-

N	Number of fluid particles	-
$n(v, t)$	Number-based density function	m^{-4}
p_0	Constant (equation 2, $p_0 = 2$)	-
ΔP	Pressure drop	Pa
q	Volume fraction distribution of the droplets	-
Q	Volume flow rate	$m^3 s^{-1}$
t	Time	s
t_b	Breakage time	s
\bar{u}	Mean velocity in a turbulent eddy	$m s^{-1}$
u_i	Interstitial velocity	$m s^{-1}$
u_s	Superficial velocity	$m s^{-1}$
$\langle [\delta u]^2 \rangle$	One-dimensional second-order longitudinal structure function	$m^2 s^{-2}$
Re_h	Hydraulic Reynolds number	-
v, v'	Droplet volume	m^3

Greek symbols

β	Constant (equation 3, $\beta = 5.2$)	-
ε	Energy dissipation rate	$m^2 s^{-3}$
$\bar{\varepsilon}$	Mean energy dissipation rate	$m^2 s^{-3}$
η	Kolmogorov length scale	m
κ	Wavenumber	m^{-1}
λ	Eddy size	m
μ	Apparent dynamic viscosity of the continuous phase	Pa s

μ_c	Dynamic viscosity of the continuous phase	Pa s
μ_d	Dynamic viscosity of the dispersed phase	Pa s
ν	Kinematic viscosity of the continuous phase	$\text{m}^2 \text{s}^{-1}$
ρ	Apparent density of the continuous phase	kg m^{-3}
ρ_c	Continuous phase density	kg m^{-3}
ρ_d	Dispersed phase density	kg m^{-3}
σ	Interfacial tension	N m^{-1}
φ	Global porosity of the static mixers	-

Supporting information

Supporting Information shows the development to adapt the kernel of Coualoulglou and Tavlarides to handle the entire energy spectrum of isotropic turbulence.

References

- (1) Ghanem, A.; Lemenand, T.; Della Valle, D.; Peerhossaini, H. Static Mixers: Mechanisms, Applications, and Characterization Methods—A Review. *Chem. Eng. Res. Des.* **2014**, *92* (2), 205–228. <https://doi.org/10.1016/j.cherd.2013.07.013>.
- (2) Nishihora, R. K.; Luhede, L.; Fritsching, U.; Novy Quadri, M. G.; Hotza, D.; Rezwan, K.; Wilhelm, M. Premix Membrane Emulsification Using Flat Microfiltration Inorganic Membranes with Tailored Structure and Composition. *J. Membr. Sci.* **2020**, *608*, 118124. <https://doi.org/10.1016/j.memsci.2020.118124>.
- (3) Ramisetty, K. A.; Pandit, A. B.; Gogate, P. R. Novel Approach of Producing Oil in Water Emulsion Using Hydrodynamic Cavitation Reactor. *Ind. Eng. Chem. Res.* **2014**, *53* (42), 16508–16515. <https://doi.org/10.1021/ie502753d>.
- (4) Alopaeus, V.; Koskinen, J.; Keskinen, K. I. Simulation of the Population Balances for Liquid–Liquid Systems in a Nonideal Stirred Tank. Part 1 Description and Qualitative Validation of the Model. *Chem. Eng. Sci.* **1999**, *54* (24), 5887–5899.
- (5) Becker, P. J.; Puel, F.; Dubbelboer, A.; Janssen, J.; Sheibat-Othman, N. Coupled Population Balance–CFD Simulation of Droplet Breakup in a High Pressure Homogenizer. *Comput. Chem. Eng.* **2014**, *68*, 140–150.
- (6) Morchain, J.; Pigou, M.; Lebaz, N. A Population Balance Model for Bioreactors Combining Interdivision Time Distributions and Micromixing Concepts. *Biochem. Eng. J.* **2017**, *126*, 135–145.

- (7) Azizi, F.; Al Taweel, A. M. Turbulently Flowing Liquid–Liquid Dispersions. Part I: Drop Breakage and Coalescence. *Chem. Eng. J.* **2011**, *166* (2), 715–725.
- (8) Lebaz, N.; Sheibat-Othman, N. A Population Balance Model for the Prediction of Breakage of Emulsion Droplets in SMX+ Static Mixers. *Chem. Eng. J.* **2019**, *361*, 625–634. <https://doi.org/10.1016/j.cej.2018.12.090>.
- (9) Lebaz, N.; Sheibat-Othman, N. Modeling Emulsification in Static Mixers: Equilibrium Correlations versus Population Balance Equations. *Chem. Eng. Technol.* **2019**, *42* (8), 1691–1701. <https://doi.org/10.1002/ceat.201900109>.
- (10) Bayraktar, E.; Mierka, O.; Platte, F.; Kuzmin, D.; Turek, S. Numerical Aspects and Implementation of Population Balance Equations Coupled with Turbulent Fluid Dynamics. *Comput. Chem. Eng.* **2011**, *35* (11), 2204–2217.
- (11) Farzi, G. A.; Rezazadeh, N.; Parsian Nejad, A. Homogenization Efficiency of Two Immiscible Fluids in Static Mixer Using Droplet Tracking Technique. *J. Dispers. Sci. Technol.* **2016**, *37* (10), 1486–1493.
- (12) Jaworski, Z.; Pianko-Oprych, P.; Marchisio, D. L.; Nienow, A. W. CFD Modelling of Turbulent Drop Breakage in a Kenics Static Mixer and Comparison with Experimental Data. *Chem. Eng. Res. Des.* **2007**, *85* (5), 753–759.
- (13) Pianko-Oprych, P.; Jaworski, Z. CFD Modelling of Two-Phase Liquid-Liquid Flow in a SMX Static Mixer. *Pol. J. Chem. Technol.* **2009**, *11* (3), 41–49.
- (14) Solsvik, J.; Jakobsen, H. A. Development of Fluid Particle Breakup and Coalescence Closure Models for the Complete Energy Spectrum of Isotropic Turbulence. *Ind. Eng. Chem. Res.* **2016**, *55* (5), 1449–1460.
- (15) Solsvik, J.; Jakobsen, H. A. A Review of the Statistical Turbulence Theory Required Extending the Population Balance Closure Models to the Entire Spectrum of Turbulence. *AIChE J.* **2016**, *62* (5), 1795–1820.
- (16) Han, L.; Gong, S.; Li, Y.; Gao, N.; Fu, J.; Liu, Z. Influence of Energy Spectrum Distribution on Drop Breakage in Turbulent Flows. *Chem. Eng. Sci.* **2014**, *117*, 55–70.
- (17) Pope, S. B. *Turbulent Flows*; IOP Publishing, 2001.
- (18) Hinze, J. O. *Turbulence*; McGraw-Hill, 1975.
- (19) Andersson, R.; Andersson, B. Modeling the Breakup of Fluid Particles in Turbulent Flows. *AIChE J.* **2006**, *52* (6), 2031–2038.
- (20) Maass, S.; Kraume, M. Determination of Breakage Rates Using Single Drop Experiments. *Chem. Eng. Sci.* **2012**, *70*, 146–164.
- (21) Ghasempour, F.; Andersson, R.; Andersson, B.; Bergstrom, D. J. Number Density of Turbulent Vortices in the Entire Energy Spectrum. *AIChE J.* **2014**, *60* (11), 3989–3995.
- (22) Solsvik, J. Turbulence Modeling in the Wide Energy Spectrum: Explicit Formulas for Reynolds Number Dependent Energy Spectrum Parameters. *Eur. J. Mech.-BFluids* **2017**, *61*, 170–176.
- (23) Niño, L.; Gelves, R.; Ali, H.; Solsvik, J.; Jakobsen, H. Applicability of a Modified Breakage and Coalescence Model Based on the Complete Turbulence Spectrum Concept for CFD Simulation of Gas-Liquid Mass Transfer in a Stirred Tank Reactor. *Chem. Eng. Sci.* **2020**, *211*, 115272. <https://doi.org/10.1016/j.ces.2019.115272>.
- (24) Karimi, M.; Andersson, R. An Exploratory Study on Fluid Particles Breakup Rate Models for the Entire Spectrum of Turbulent Energy. *Chem. Eng. Sci.* **2018**, *192*, 850–863.
- (25) Ashar, M.; Arlov, D.; Carlsson, F.; Innings, F.; Andersson, R. Single Droplet Breakup in a Rotor-Stator Mixer. *Chem. Eng. Sci.* **2018**, *181*, 186–198.

- (26) Karimi, M.; Andersson, R. Dual Mechanism Model for Fluid Particle Breakup in the Entire Turbulent Spectrum. *AIChE J.* **2019**, *65* (8), e16600.
- (27) Davidson, P. *Turbulence: An Introduction for Scientists and Engineers*; Oxford University Press, 2015.
- (28) Coualaloglou, C. A.; Tavlarides, L. L. Description of Interaction Processes in Agitated Liquid-Liquid Dispersions. *Chem. Eng. Sci.* **1977**, *32* (11), 1289–1297.
- (29) Castellano, S.; Carrillo, L.; Sheibat-Othman, N.; Marchisio, D.; Buffo, A.; Charton, S. Using the Full Turbulence Spectrum for Describing Droplet Coalescence and Breakage in Industrial Liquid-Liquid Systems: Experiments and Modeling. *Chem. Eng. J.* **2019**, *374*, 1420–1432. <https://doi.org/10.1016/j.cej.2019.06.032>.
- (30) Vankova, N.; Tcholakova, S.; Denkov, N. D.; Vulchev, V. D.; Danner, T. Emulsification in Turbulent Flow: 2. Breakage Rate Constants. *J. Colloid Interface Sci.* **2007**, *313* (2), 612–629.
- (31) Kolmogorov, A. N. Dissipation of Energy in Locally Isotropic Turbulence. In *Dokl. Akad. Nauk SSSR*; 1941; Vol. 32, pp 16–18.
- (32) Narsimhan, G.; Gupta, J. P.; Ramkrishna, D. A Model for Transitional Breakage Probability of Droplets in Agitated Lean Liquid-Liquid Dispersions. *Chem. Eng. Sci.* **1979**, *34* (2), 257–265.
- (33) Hsia, M. A.; Tavlarides, L. L. Simulation Analysis of Drop Breakage, Coalescence and Micromixing in Liquid-Liquid Stirred Tanks. *Chem. Eng. J.* **1983**, *26* (3), 189–199.
- (34) Raikar, N. B.; Bhatia, S. R.; Malone, M. F.; Henson, M. A. Experimental Studies and Population Balance Equation Models for Breakage Prediction of Emulsion Drop Size Distributions. *Chem. Eng. Sci.* **2009**, *64* (10), 2433–2447.
- (35) Procedure for Estimation and Reporting of Uncertainty Due to Discretization in CFD Applications. *J. Fluids Eng.* **2008**, *130* (078001). <https://doi.org/10.1115/1.2960953>.
- (36) Kumar, J.; Warnecke, G.; Peglow, M.; Heinrich, S. Comparison of Numerical Methods for Solving Population Balance Equations Incorporating Aggregation and Breakage. *Powder Technol.* **2009**, *189* (2), 218–229.
- (37) Chabanon, E.; Sheibat-Othman, N.; Mdere, O.; Valour, J. P.; Urbaniak, S.; Puel, F. Drop Size Distribution Monitoring of Oil-in-Water Emulsions in SMX+ Static Mixers: Effect of Operating and Geometrical Conditions. *Int. J. Multiph. Flow* **2017**, *92*, 61–69. <https://doi.org/10.1016/j.ijmultiphaseflow.2017.03.001>.
- (38) Theron, F.; Le Sauze, N. Comparison between Three Static Mixers for Emulsification in Turbulent Flow. *Int. J. Multiph. Flow* **2011**, *37* (5), 488–500.
- (39) Hert, S. C. D.; Rodgers, T. L. On the Steady-State Drop Size Distribution in Stirred Vessels. Part I: Effect of Dispersed Phase Viscosity. *AIChE J.* **2018**, *64* (9), 3293–3302. <https://doi.org/10.1002/aic.16171>.
- (40) Hert, S. C. D.; Rodgers, T. L. On the Steady-State Drop Size Distribution in Stirred Vessels. Part II: Effect of Continuous Phase Viscosity. *AIChE J.* **2019**, *65* (5), e16556. <https://doi.org/10.1002/aic.16556>.
- (41) Al Taweel, A. M.; Li, C.; Gomaa, H. G.; Yuet, P. Intensifying Mass Transfer Between Immiscible Liquids: Using Screen-Type Static Mixers. *Chem. Eng. Res. Des.* **2007**, *85* (5), 760–765. <https://doi.org/10.1205/cherd06180>.

Table of Contents Graphic

